IEEE Access
Multidisciplinary | Rapid Review | Open Access Journal

Received 8 July 2022, accepted 30 July 2022, date of publication 5 August 2022, date of current version 12 August 2022.

*Digital Object Identifier 10.1109/ACCESS.2022.3196919*

RESEARCH ARTICLE

# Computationally Efficient Surrogate-Based Magneto-Fluid-Thermal Numerical Coupling Approach for a Water-Cooled IPM Traction Motor

**AHMED S. ABDELRAHMAN, (Member, IEEE), AND BERKER BILGIN, (Senior Member, IEEE)**
McMaster Automotive Resource Centre (MARC), McMaster University, Hamilton, ON L8P 0A6, Canada

Corresponding author: Ahmed S. Abdelrahman (abdela48@mcmaster.ca)

**ABSTRACT** This paper proposes a computationally-efficient electromagnetic (EM)-computational fluid dynamics (CFD) coupling approach for a water-cooled Interior Permanent Magnet (IPM) motor. The numerical simulation of multiple fluids and their interaction with solid parts can be challenging. The proposed approach relies on the heat transfer coefficient (HTC) decomposition of different fluids/coolants inside the machine to generate an HTC look-up table (LUT) as a function of the coolant inlet flow rate. The HTC-LUT is then utilized as a surrogate model for the stationary coolant to decouple the fluid-to-fluid interaction and, hence, expedite the iterative approach. This reduces the computational time by almost two-thirds as compared to the multiple fluid approach while preserving the fidelity of the model. Additionally, the proposed approach formulates the correlation between the rotor speed, coolant flow rate, convective heat transfer coefficients, and the temperature rise, particularly for hot-spot locations in the end-windings. This approach uses a two-dimensional EM model coupled with a three-dimensional fractional CFD model. Thus, it reduces the computational cost and retains the model simplicity. The viability of the proposed coupling approach is also validated through lumped parameter thermal network (LPTN) analytical approach. The results from both approaches under different cooling conditions, flow rates, and current densities are in a good agreement.

**INDEX TERMS** Computational fluid dynamics (CFD), dual-three phase machine, finite-element analysis (FEA), hairpin windings, interior permanent magnet (IPM), synchronous machine, lumped-parameter thermal network (LPTN).

## I. INTRODUCTION

Towards ameliorating and protecting the environment from the harmful emissions that stems from gasoline vehicles, automotive manufactures are putting numerous efforts to develop and deploy an energy-efficient transportation focusing on electric vehicles. In order to meet and fulfill the stringent packaging constraints stimulated by the U.S. department of energy (DOE) for the power electronics and electric motors, increasing the power density has become a major target. Since the electric motor is among the crucial parts for enhancing the overall efficiency of the vehicle, its power density is anticipated to reach 50 kW/L by 2024 accounting for an 89% reduction of its current volume [1]. Operating at such high-power density translates directly into an increase in loss density, meaning a smaller area for heat dissipation [2], [3].

In IPM motors, design for a compact envelope without having a rigorous and optimized cooling system results in rapid temperature rise. This would accordingly result in poor electromagnetic performance as the properties of magnetic materials are temperature-dependent. Excessive temperature is detrimental to the motor performance especially from the structural standpoint since high temperature adversely affects stresses acting on the rotor. In other words, the thermal performance can be considered as the limiting factor

The associate editor coordinating the review of this manuscript and approving it for publication was Zhong Wu.

for investigating the electric vehicle performance. Therefore, accurate calculation of the motor temperature and its effect on the electromagnetic performance is essential to determine the motor's throughput. In order to advance high-power traction motor design, the machine's thermal limits should be accurately calculated for the given cooling approach. That still remains a major challenge for motor design engineers due to various factors. For example, there are different heat sources in the motor with irregular geometries causing non-uniform heat generation. Interaction between rotational flows (e.g. the air flowing in the air gap region), and non-rotating flows (e.g. coolant flowing in the motor frame through the cooling jacket) is another factor that makes it challenging to analyze the thermal limits. Finally, the choice of different thermal exchange modes, such as conduction, convection, and radiation should be taken into consideration in the modeling and simulation of an electric motor [4].

In electric motor design, a pre-defined current density is conventionally utilized as a surrogate to ensure that the operation is below the permissible temperature limit [5]. This method can be inaccurate and insufficient especially with high-power high-speed traction motors. Different techniques based on analytical and best practices have also been introduced in the literature to determine the maximum current density [6], [7]. Several papers adopted lumped parameter thermal network (LPTN) for achieving a fast coupling approach and to determine the maximum allowable winding current density for maximum torque production [6], [8]–[10]. In [11], an improved LPTN EM-thermal coupling approach encompassing stress constraints was implemented for induction machines. Additionally, the design of a surface permanent magnet motor using an analytical multi-physics approach was investigated in [12]–[14]. A similar approach was utilized to analyze an interior permanent magnet motor [15], [16]. In these LPTN-based methods, several assumptions have been made to simplify the analytical model and make it computationally efficient. For example, the rotor losses have been ignored in [14], [15]. Also, the saturation in the magnetic core has been ignored in [16] which, in turn, compromises the fidelity of the solution.

A more advanced non-linear multi-physics analytical model has been developed in [17] that takes the local saturation into consideration, especially near the rotor bridges. However, the calculation of the thermal resistances used in the thermal network had lower accuracy because an oversimplified technique was used to determine the HTCs. On the other hand, a coupled EM-thermal finite element analysis (FEA) model has been introduced in [18]. This method proposes a new FEA-based coupling approach for EM and thermal analysis, but it fails to include the rotational air effect. Hence, speed-dependent convective HTCs, especially for end-windings, are ignored.

In this paper, an EM-CFD coupling approach using a stationary coolant HTC-LUT as a surrogate is adopted. First, an HTC-LUT is generated in the CFD model by utilizing the loss data from the EM FEA model at a specified initial temperature. By providing this HTC-LUT of the stationary coolant, decoupling for the fluid-to-fluid interaction is established. The Moving Reference Frame (MRF) technique is then used to solve for the rotational effects in the airgap at different operating speeds. Another HTC-LUT is then obtained as a function of the velocity of the local air passing through the end-windings. The proposed approach is validated with an LPTN analytical model. In the LPTN model, the thermal resistances are calculated using the HTC derived from the proposed EM-CFD coupling method.

**TABLE 1. Heat sources of the machine at 1.00 p.u. current density.**

| Heat Sources | Base Speed | Maximum Speed |
|---|---|---|
| Copper losses [kW] | 1.47 | 3.05 |
| Stator core losses [kW] | 0.603 | 1.75 |
| Rotor core losses [W] | 8.58 | 32.3 |
| Magnets losses [W] | 6.92 | 6.76 |
| Mechanical losses [kW] | 0.329 | 2.247 |
| Total [kW] | 2.416 | 7.09 |

## II. MOTOR MODEL AND LOSSES

A 300 kW 96-slot 8-pole delta-shape IPM motor designed for a traction application is used for this analysis. Fig. 1 shows the cross-section view and the main dimensional parameters of the motor. The base speed of the motor is 6500 rpm and the maximum speed is 17,000 rpm. The torque-speed and power-speed characteristics of the motor for the maximum load condition obtained from the electromagnetic FEA analysis are shown in Fig. 2. The maximum torque at the base speed is 450 N.m and the maximum torque at the maximum speed is 95 N.m. In the proposed EM-CFD coupling approach, a two-dimensional (2D) finite element model is used for the electromagnetic modeling and analysis of the motor. As shown in Fig. 1, the dual three-phase motor is designed with hairpin wave winding. Since half set of the windings are shifted by $30^{o}$ electrical to implement the dual three-phase operation, the winding distribution factor is 0.9659 while it would be 0.9577 for its three-phase counterpart [19], [20]. Thus, the dual three-phase winding is advantageous in terms of a higher distribution factor for the same slot/pole combination.

Fig. 3 shows two coils of phase A and Phase D with their elementary windings. Layer 8 of slot 2 indicates the beginning of the elementary winding of Phase A while layer 7 of slot 14 marks its first end. Then, it loops back to layer 8 of slot 1 where a slot change occurs and moves forward again to slot 13 at its $7^{th}$ layer. A layer change denoted by a black line in Fig. 3 is then appeared at this position for which the winding shifts to slot 2 at its $6^{th}$ layer. This pattern continues until the first elementary winding completely ends at layer 1 of slot 13. The same procedure applies to other phases. Different losses of the machine under study at the base and maximum speed operating conditions are also outlined in Table 1 [21].

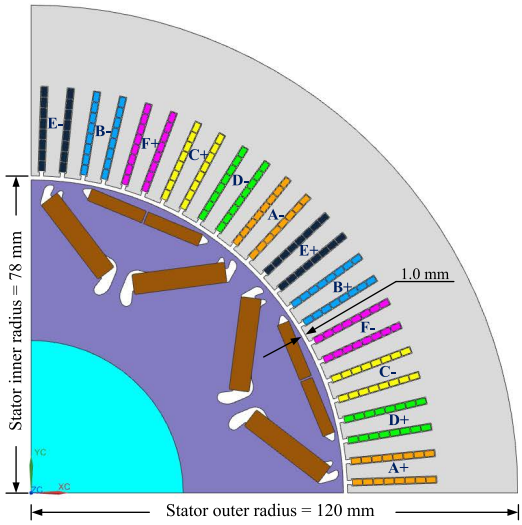


**FIGURE 1.** Cross section view and the main dimensions of the analyzed dual three-phase 96-slot 8-pole IPMSM (stack length: 100mm, slot fill factor: 0.709).

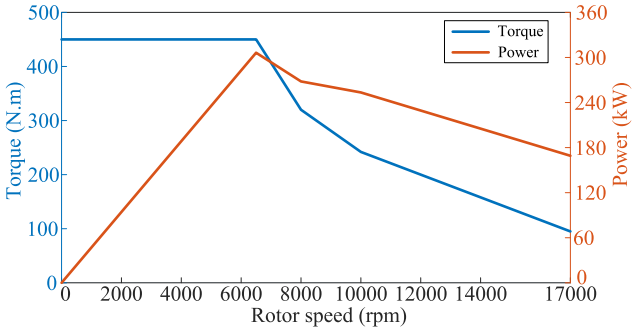


**FIGURE 2.** Torque-speed and power-speed characteristics of the traction motor.

## III. CFD MODELING FOR THE LIQUID-COOLED TRACTION MOTOR CONSIDERING ROTATIONAL EFFECTS

A thermal CFD-based modeling approach is utilized to develop a comprehensive thermal analysis considering rotational effect of the rotor at different operating speeds. CFD is used to calculate and predict the airflow and heat transfer coefficients of the motor surfaces. It takes the turbulent model and rotational effects into consideration to have an accurate representation of the problem. As depicted in Fig. 4, a 16-channel axial-rib water-cooling jacket is applied to dissipate the heat generated in the dual three-phase motor [22]–[24]. The cross-sectional view of the motor construction is shown in Fig. 5. It highlights the main parts of the motor including the water-jacket inlet and outlet, and the air regions.

The three-dimensional model used in the CFD analysis is for one-eighth of the circumferential geometry and the entire length in the axial direction. Fig. 6 depicts the fluid regions inside the machine model. The cooling medium is a water jacket with Ethylene Glycol Water (EGW) (50/50) coolant in the outer housing. Since the rotational influence at different speeds is considered, the air region depicted by purple color in Fig. 5 (rotating rotor air volume among the stator, rotor, and the motor outer frame) is divided into two main regions: stator air region and rotor air region as shown in Fig. 6. This division is necessary to apply the moving reference frame method. The stator air region in Fig. 6 is attached to the stator. It is stationary in nature meaning that it does not move with the rotor rotation. The rotor air region in Fig. 6 is the moving air region which is associated with the rotor. It moves at the same speed as the rotor rotation speed.

Fig. 7 shows the main stages of setting up the CFD model. First, a detailed geometry with a pre-defined named-selection in Ansys Spaceclaim platform is established and checked for any overlapping surfaces. Then, the mesh module is used to define the fluid/solid interfaces. A shared topology is used for the water-cooling jacket to simplify the mesh. In a shared topology, faces between touching or intersecting surfaces are shared to achieve a conformal mesh. Then, the boundary conditions such as the coolant inlet flow rate, initial coolant temperature, and the periodicity of the model are defined. The temperature-dependent material properties are then integrated into the model. After running the model with the proper viscous model/solver, the results are post-processed.

### A. MESHING FOR CFD ANALYSIS WITH ROTATIONAL DYNAMICS

The meshing is a crucial aspect in CFD simulation since various meshing parameters including the number of elements and their shapes (tetrahedral, polyhedral, and hexahedral) as well as the number of nodes have a significant impact on the accuracy and the solution convergence. The unstructured conformal mesh approach is adopted in this study. Fig. 8 shows the surface meshing of the housing cooling jacket where the element types and their connectivity are not predefined. This reduces the computational cost drastically. This unstructured mesh consists of tetrahedral, hexahedral, and arbitrary polyhedrals elements. This approach is preferable as it allows using a semi-automated meshing. Besides, it helps to resolve the boundary layers efficiently by using high aspect ratio prism cells [25].

Fig. 9 shows how the volume polyhedral meshing is applied to the housing water-jacket. As illustrated in Fig. 9, the inflation layers should be applied at the inlet and outlet to capture the physics near the wall. This improves the solution accuracy of the turbulent coolant flow. Fig. 9 also shows the solid-fluid volume meshing. It can be observed that the fluid mesh area for the water jacket is denser than the solid area for the housing to increase the solution accuracy of the turbulence equations. Polyhedral mesh is used both for the fluid and solid domains to maintain the conformal mesh [26]. For a viscous flow bounded with solid boundaries, it is essential to cluster a large number of small cells within the physical boundary so that the actual flow physics is appropriately accounted [27]. Thus, the polyhedral mesh is selected for solids with a mesh size of 4.0 mm and refinements at the surfaces is chosen as the appropriate mesh settings. Mesh refinement is the concept of a stretched grid in the vicinity of the domain walls.

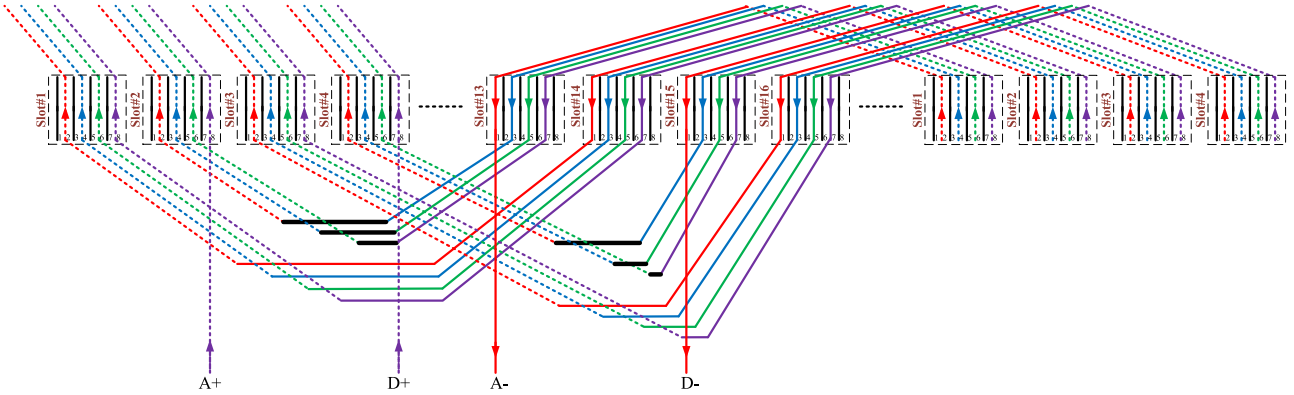


**FIGURE 3.** Winding configuration of the 96-slot 8-pole dual-three-phase motor (shown for two coils of phases A and D with the start and end connections highlighted).

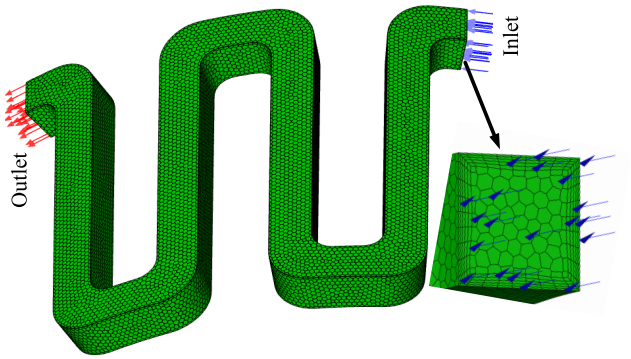


**FIGURE 4.** 16-channel axial-rib water-cooling jacket applied in the dual-three phase motor (1/8$^{th}$ partial model is utilized to reduce the computational cost).

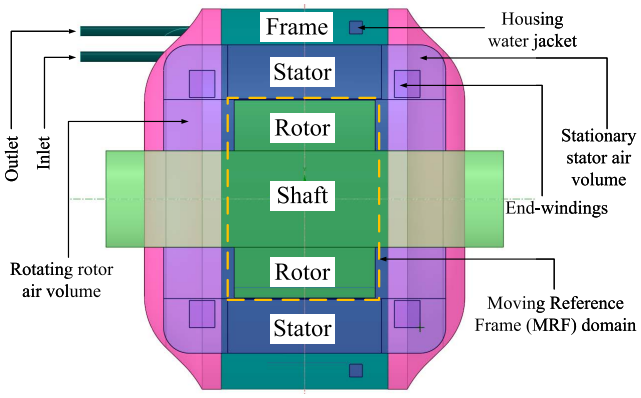


**FIGURE 5.** Cross sectional view of the dual three-phase motor for CFD analysis.

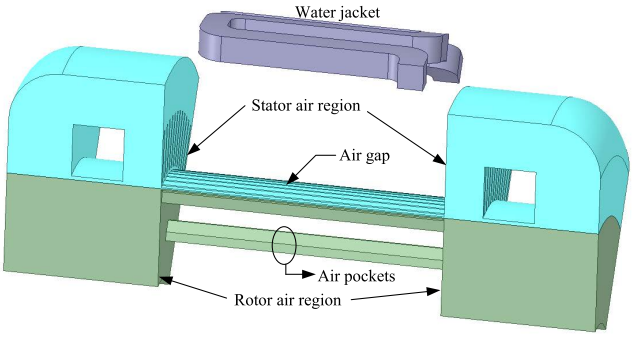


**FIGURE 6.** Fluid regions inside the motor and decomposition of the rotating rotor air volume into stator and rotor air regions.

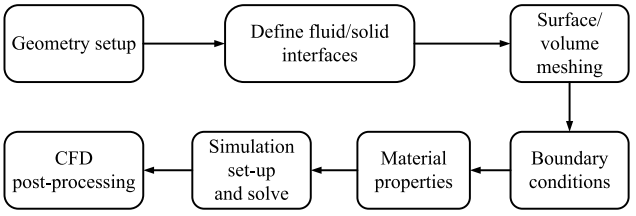


**FIGURE 7.** CFD detailed setup workflow inside Ansys Workbench Fluent module.

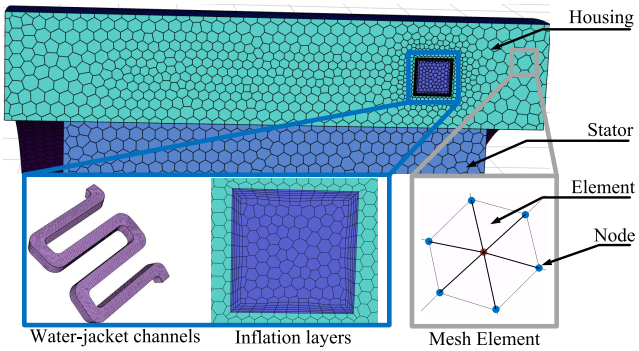


**FIGURE 8.** Surface polyhedral meshing of the housing water-jacket.

Orthogonality and skewness are the most important metrics to evaluate and assess the quality of the generated mesh. The proximity of the optimal angle, which is 90° for quadrilateral faced elements and 60° for triangular faced elements, to the adjacent element faces/edges is determined by calculating the orthogonality. Therefore, a good mesh should have an orthogonality value as close as possible to one. The similarity between a certain face or cell to its ideal shape is known as skewness. Thus, skewness value of zero indicates that

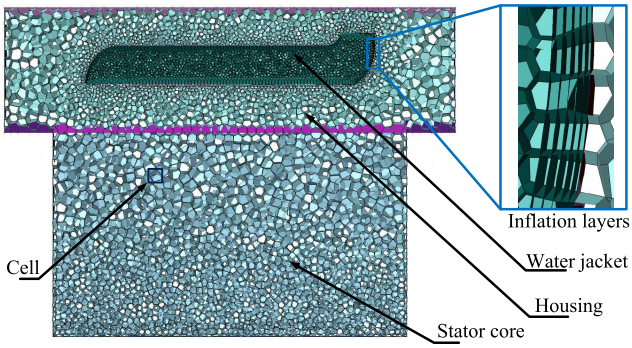


**FIGURE 9.** Volume polyhedral meshing of the housing water-jacket.

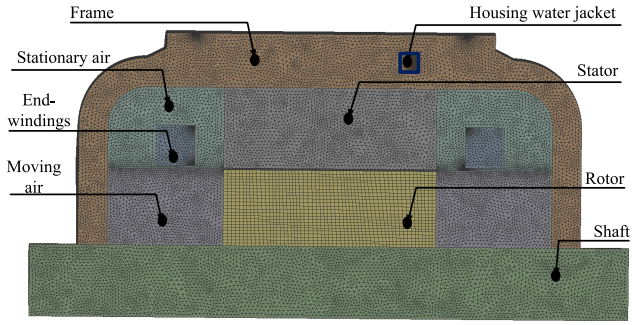


**FIGURE 10.** Mesh of the motor model for CFD analysis generated in Ansys meshing module (600,718 mesh nodes and 2,720,312 mesh elements).

the cell matches to its ideal condition. For example, when skewness is zero, an equilateral triangle would be constructed with triangular-faced elements and a square would be constructed with quadrilateral-face elements. When skewness is one, it indicates that a cell is completely degenerated. A good mesh should have a maximum skewness value not higher than 0.95 (0.98 is the maximum admissible value in Ansys Fluent) and an average skewness less than 0.25 [26].

Fig. 10 illustrates the numerical grid mesh generated for the entire motor model. It can be observed that the mesh in the fluid domain, highlighted with a blue square in Fig. 10, is denser than the solid domains. This is essential to capture the near wall physics [28], which is discussed next.

### B. WALL TREATMENT APPROACH AND NEAR WALL MODELING

The set of near-wall modeling assumptions for a turbulence model is defined as the wall treatment. Since the friction coefficients and HTCs are supposed to be accurately anticipated near the walls, it is imperative to carefully select the proper combination of the near wall mesh resolution and the wall treatment to obtain a logarithmic boundary layer profile which means that the wall functions correctly predict the boundary layer. This section will discuss the assumptions and the conditions that will lead to this proper selection.

Firstly, a no-slip condition is always assumed at the wall. This means that, the velocity of the fluid relative to the wall is almost zero. For the turbulence model, a boundary layer

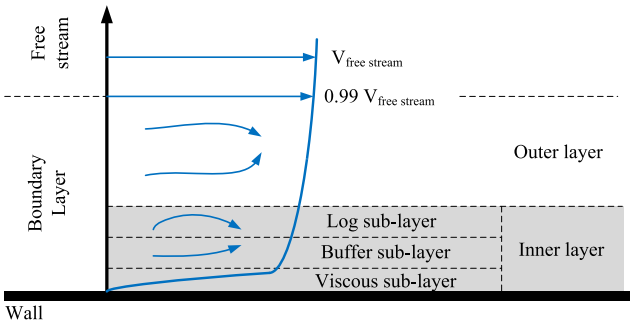


**FIGURE 11.** Velocity boundary layer development near the wall in convection heat transfer [30], [31].

is formed at a certain distance from the leading edge of the surface where inertial forces are dominant. As indicated in Fig. 11, the turbulent boundary layer consists of three main sub-layers which are formed in the direction normal to the wall: viscous sub-layer, buffer sub-layer, and log or fully-turbulent sub-layer. In the viscous sub-layer, viscous stress is dominant and the flow is mainly laminar in nature. The buffer sub-layer is a transitional layer in between the viscous sub-layer and the log sub-layer. In the buffer sub-layer, both viscous and turbulent stresses exist. Hence, a fine mesh is necessary in both layers to capture a steep flow-velocity gradient near the wall. Since the turbulent stress is dominant in the log sub-layer, it requires a course mesh to capture smaller velocity gradient away from the wall.

There are generally two different approaches for solving the near-wall boundary layer: the wall function approach and the near-wall model approach. In the proposed CFD model, the wall function approach and the near-wall model approach are adopted in a hybrid way with inflation layers. This improves the accuracy and solves the entire boundary-layer. In order to quantify the accuracy of the near-wall modeling, the $y^+$ wall treatment approach is used [29]. This approach is mainly used for turbulence models as the mesh varies in quality depending on the component of the electric machine. In the $y^+$ wall treatment approach, the $y^+$ value is a non-dimensional distance. It is determined based on the local cell fluid velocity. The $y^+$ value is used to measure the distance of the inner layer to the wall and, hence, it defines the nature of the flow, either laminar or turbulent, according to the wall adjacent cells. It is often used in CFD to describe if the mesh is fine or coarse.

### C. MODELING OF SOLID PARTS

The most crucial aspect of the solid parts meshing is how to handle the interfaces between them. This means the way that the nodes and elements across the interfaces are being connected to each other. Therefore, there are two common ways to create the meshing of the solid-to-solid interfaces; the conformal meshing and the non-conformal meshing. The conformal mesh adopted in the CFD model ensures proper mapping of both surfaces. However, the downside appears when a large body is in contact with a complex shape,

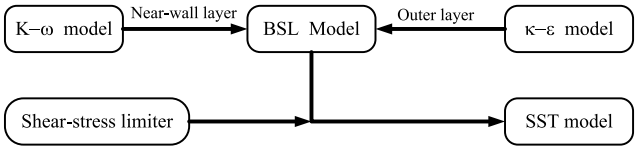


**FIGURE 12.** Block diagram representation of the SST turbulence model: shear-limited BSL model.

or a very small geometry. This causes the larger body get re-meshed with a fine mesh similar to contacting a complex shape or a small geometry. Hence, it leads to an increase in the number of cells.

### D. FLUID-SOLID HEAT TRANSFER

The Conjugate Heat Transfer (CHT) method is implemented to account for the heat transfer between fluids and solids with incorporation of the Shear Stress Transport (SST) turbulent model. Fig. 12 illustrates the block diagram of the SST turbulence model as a shear-limited Baseline (BSL) model. The SST model is a blend of both k-$\omega$ and k-$\epsilon$ integrated with shear-stress limiter. This approach fixes the over flow predictions associated with the k-$\omega$ and k-$\epsilon$ models [32].

The motor can operate with different mass flow rates, depending on the operating condition. For high mass flow rates, the flow is usually turbulent. As depicted in Fig. 12, a turbulence model is chosen for the cooling flow for all flow rates, because the chosen k-$\omega$ SST model can calculate the flow conditions both for laminar and transitional flow. Another reason for choosing a turbulence model for laminar conditions is that even though the flow may be laminar in the straight channels of the water-cooling jacket, the jacket has 180° bends as shown in Fig. 4, and the flow tends to be turbulent.

## IV. DEVELOPMENT OF HTC-LUTs AND MRF APPROACH

### A. HEAT TRANSFER COEFFICIENT (HTC) LOOK-UP TABLES (LUTs)

In order to confirm that the modeling of the housing water-cooling jacket is adequate, residual plot generated by Ansys CFD can be used [30]. The convergence of the solution is confirmed since all the residuals were descending and they all eventually settled, especially the continuity residual. The velocity streamlines are shown in Fig. 14. The maximum coolant velocity obtained is 4.72 m/s for 12 LPM coolant flow rate.

The main objective of simulating the water-jacket without considering the rotational effect at first is to generate the HTC-LUT as a function of the flow rate. The LUT is then utilized with the main CFD simulation. Using the HTC-LUT as a surrogate for the main CFD simulation helps reducing the computational cost since it utilizes separate simulations for the coolants and decouples the fluid-to-fluid interaction. In order to generate the HTC-LUT, the first step is to calculate the wall heat flux ($\dot{Q}_{\text{conv}}$) as shown in Fig. 15. Then the wall surface temperature ($T_s$) and the fluid temperature ($T_f$) are calculated in Ansys Fluent. A look-up table for the convective heat transfer coefficients is generated by applying (1) between the moving fluid (coolant) and the

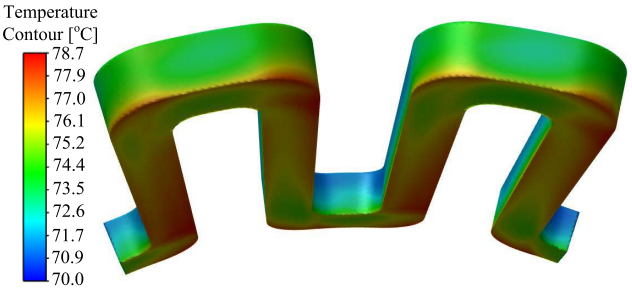


**FIGURE 13.** Water-cooling jacket wall-temperature contour for 12 LPM flow rate.

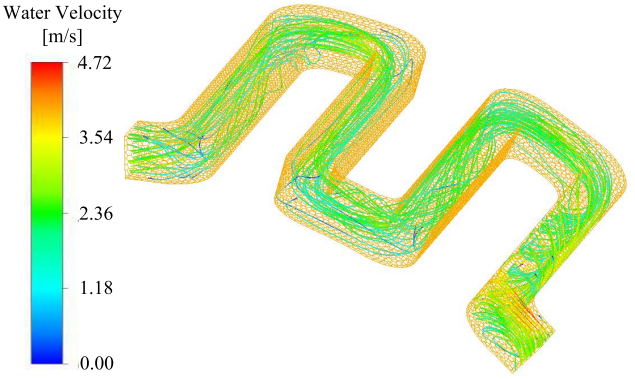


**FIGURE 14.** Water-cooling jacket velocity stream for 12 LPM flow rate.

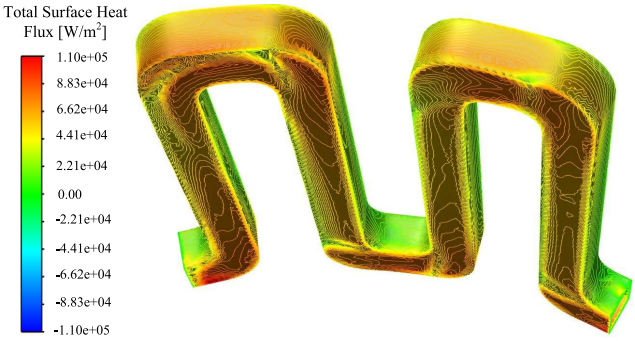


**FIGURE 15.** Water-cooling jacket heat flux contour for 12 LPM flow rate.

**TABLE 2.** HTC-LUT for water cooling jacket.

| Coolant Flow Rate [LPM] | HTC [W/m$^2$/°C] | Coolant Flow Rate [LPM] | HTC [W/m$^2$/°C] |
|---|---|---|---|
| 1 | 442.53 | 7 | 781.43 |
| 2 | 494.49 | 8 | 844.25 |
| 3 | 548.25 | 9 | 908.88 |
| 4 | 603.83 | 10 | 975.33 |
| 5 | 661.22 | 11 | 1043.58 |
| 6 | 720.42 | 12 | 1113.65 |

solid (cooling jacket):

$$h = \dot{Q}_{conv}/(T_s - T_f). \quad (1)$$

In Fig. 15, the negative values of the heat transfer indicate the existence of vortex or zone of re-circulation due to lower values of Nusselt number as the fluid speed slows down. However, this is seldom in our problem since the flow rate is high.

Table 2 shows the HTC values calculated at different flow rates for the water cooling jacket. Average values of HTCs are considered in all calculations and LUT generation. It can be observed that the HTCs for water-cooling jacket walls increase with increasing coolant flow rate. This is due to the advection effect. Advection means that the fluid particles capture the heat and move forward leaving space for the incoming fluid particles to occupy the same space and extract the heat. Therefore, if the velocity of the fluid increases, the rate of advection increases. This, in turn, increases the rate of convection and the HTC.

### B. INTERNAL ROTATING AIR AND MOVING REFERENCE FRAME APPROACH

In order to model the air flow inside the motor as a steady state problem, a moving non-inertial reference frame has to be adopted. Hence, the unsteady problem, resulted from solving with respect to the moving parts that is usually difficult to converge, can be solved via a steady state stationary reference frame for which the air flow problem can easily converge. However, in this case, the governing equations of the air flow have to be modified to account for additional acceleration terms associated with the transformation process from the stationary reference frame to the moving reference frame. Since there is almost no significant outer air flow, there was no need to have an outer air domain region and, hence, it has not been modeled. However, the outer walls of the housing have been identified and a free stream temperature boundary condition with an initial heat transfer coefficient have been assigned to all the outer housing walls.

For an electric machine, splitting the computational domain into two regions provides simplicity in modeling and solution convergence. The first domain rotates synchronously with the rotor and the second domain is fixed with the stator, as it was shown in Fig. 6. This is called the Moving Reference Frame (MRF) approach. The steady state model of the air flow is represented through the MRF approach where the transient effects are ignored. Rotor rotation is considered through centrifugal forces not with physical rotation. Therefore, walls are not rotating physically in the CFD analysis. The MRF approach is computationally less expensive in comparison to the the sliding mesh method [33].

Fig. 17 shows the air velocity contour inside the machine at the base speed and it illustrates how the computational domain is separated into two regions. It can be observed that the velocity in the stator air region in Fig. 16 is maintained at zero speed. The maximum velocity is attained in small cross sectional areas in the flux barrier region. The air

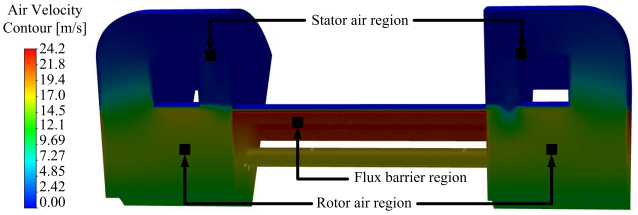


**FIGURE 16.** Air velocity contour inside the machine at the base speed operation.

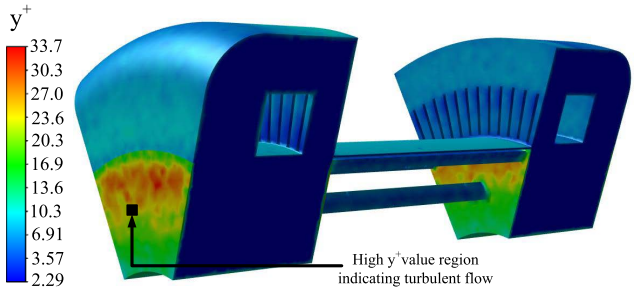


**FIGURE 17.** $y^+$ contour plots near the walls at the base speed operation.

**TABLE 3.** Correlation between motor speed, local air velocity, and end-windings HTC.

| Motor Speed (rpm) | Local Air Velcoity (m/s) | End-windings HTC [W/m$^2$/°C] |
|---|---|---|
| 3000 | 17.69 | 43.24 |
| 5000 | 29.29 | 62.88 |
| 7000 | 40.92 | 82.57 |
| 9000 | 52.67 | 102.46 |
| 11000 | 64.31 | 122.17 |
| 13000 | 75.99 | 141.94 |
| 15000 | 86.98 | 160.54 |
| 17000 | 94.75 | 173.70 |

velocity decreases gradually in the rotor air region as depicted in Fig. 16.

As discussed earlier, $y^+$ wall treatment approach has been used in order to quantify the accuracy of the near-wall modeling. Fig. 17 shows the $y^+$ contour on a selected wall. In order to indicate the effectiveness of the $y^+$ approach, the $y^+$ values are calculated in the centre of the mesh cell adjacent to the selected wall. $y^+$ values greater than 30 can be observed in the selected wall in Fig. 17. These high $y^+$ values indicate that the governing equations of the turbulent flow are correctly solved. The local air velocities, at different motor speeds, are calculated around the end-windings in the CFD analysis. A step size of 2000 rpm for the motor speed is adopted to capture the increasing behavior of the HTCs. The temperature contours of the IPM motor demonstrated that the hotspot is consistently located in the end-windings. Hence, estimating the HTC for the end-windings is crucial; however, it is quite challenging as well. It was assumed that the end winding outer surfaces are flat with no bending regions [34]. Therefore, the empirical formula in (2) proposed

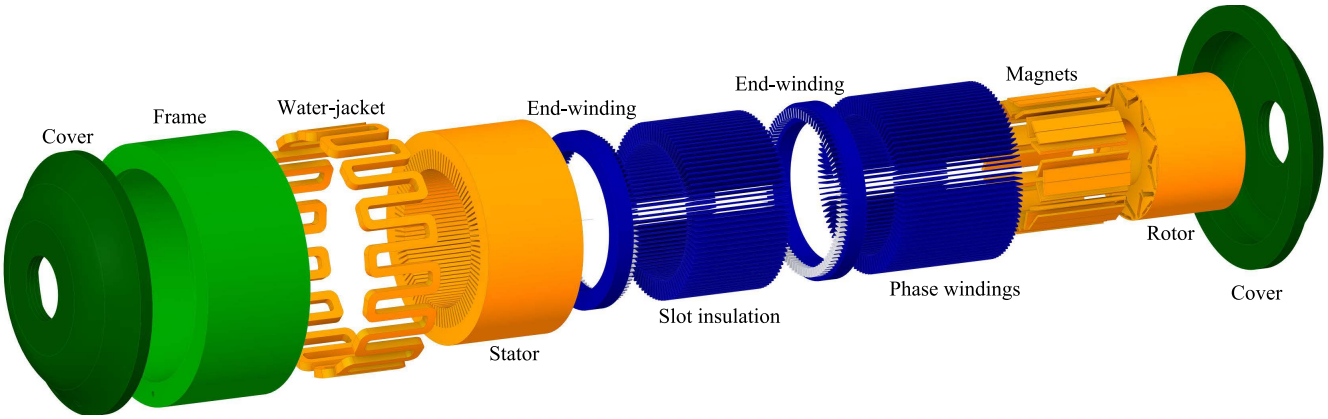


**FIGURE 18.** Exploded view of the IPM machine geometry with a 16-channel housing water-jacket and a simplified end-winding geometry.

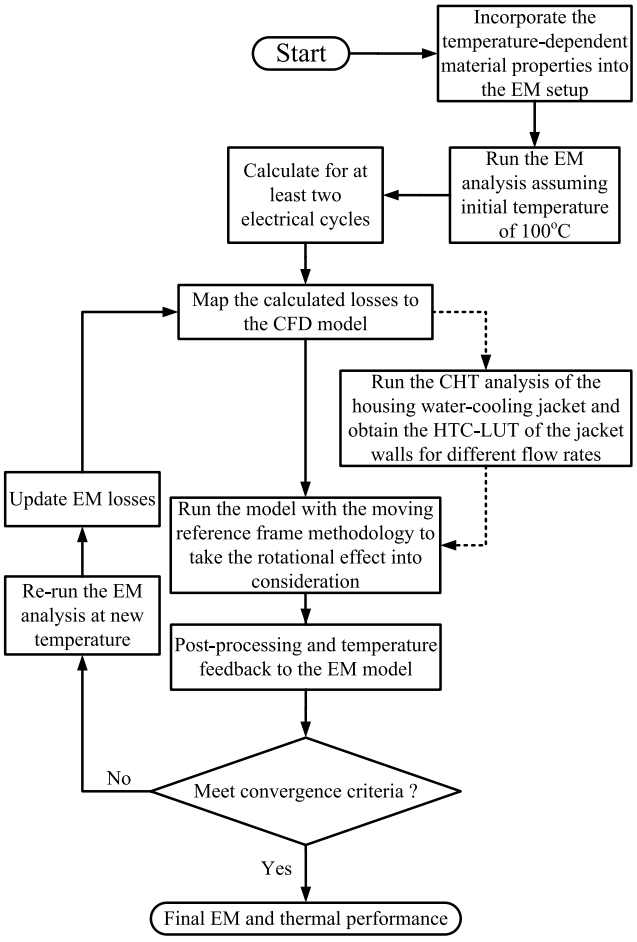


**FIGURE 19.** Flowchart of the proposed HTC-LUT surrogate-based model.

in [34] is considered here to estimate the HTC of the end-windings. Table 3 shows the correlation between the motor speed, local air velocity ($v$), and the HTC of the end-windings ($h_{EW}$). It can be observed that the HTC of the end-windings increases with speed. This indicates that, as the heat transfer coefficient increases, the power that can be dissipated by the end-windings to the local air also increases.

$$h_{EW} = 13.29 + 1.693v. \tag{2}$$

## V. THE PROPOSED EM-CFD COUPLING WITH THE HTC-LUTs AS SURROGATE MODEL

In this section, the developed HTC-LUTs are integrated in the CFD model of the dual three-phase motor. The motor parts used in the CFD analysis are shown in the exploded view in Fig. 18. It can be observed that all motor parts are included in the model. A simplified end-winding geometry is used to facilitate the meshing process without affecting the output temperature gradient. The CFD model is coupled with the EM model of the motor via a two-way iterative feedback connection and run for multiple iterations until a steady-state temperature is reached. This enables calculating the motor performance metrics, such as average torque, copper and core losses, for nonhomogenous temperature distribution in the motor core and windings for different coolant flow rates and current levels. The results are then compared with the ones from the EM model where a constant temperature was applied.

### A. COUPLED EM-CFD ANALYSIS FLOW CHART

The proposed EM-CFD flowchart is demonstrated in Fig. 19. It is setup and simulated in Ansys Workbench. The initial temperature of the motor for EM analysis is set to 100°C. The coolant temperature is set at 70°C. Temperature-dependent material properties are incorporated in the coupled model and their initial temperature was also set as 100°C. The two-dimensional EM model is then executed for at least two electrical cycles as this is the minimum requirement for the core losses to reach to a steady-state. The average value of the core loss waveform in the second electrical cycle is used when mapping the losses to the CFD model. In the proposed HTC-LUT decomposition approach, the core loss is applied to two separate three-dimensional CFD thermal models. The first model represents the water cooling jacket. It is executed only once to generate the HTC-LUT for the

**TABLE 4. Material properties used in the machine model.**

| Material | $\rho$ [kg/m$^3$] | $c_p$ [J/kg-K] | $\lambda$ [W/m-K] |
|---|---|---|---|
| Ethylene Glycol Water (50/50) | 998.2 | 4182 | 0.6 |
| Air | 1.1 | 1006 | 0.0531 |
| Cast-iron | 8030 | 502 | 55 |
| Copper | 8978 | 381 | 387.6 |
| Magnet (NdFeB) | 7600 | 502.416 | 7.6 |
| Insulation | 2000 | 502 | 10 |
| Steel | 8030 | 502.48 | 16.27 |

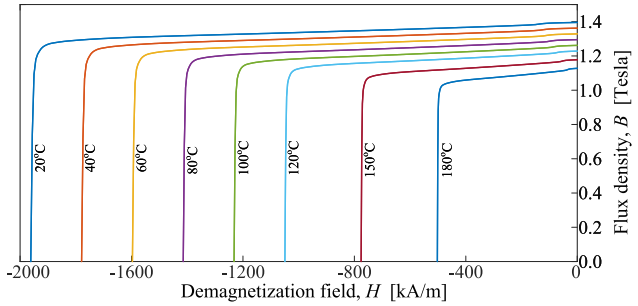


**FIGURE 20. Temperature-dependent *B-H* curve of the magnet material.**

cooling jacket surfaces, as discussed in Section IV. The rotor is stationary in this case. The second model incorporates the generated HTC-LUT with a moving rotor modeled with the MRF technique.

The EM model is connected to the CFD model via a two-way iterative feedback connection. After obtaining the temperature gradient, the temperature is mapped back to the EM model to update the material properties and calculate the losses for the updated temperature gradient. Then the calculated losses in the EM model are applied as inputs to the CFD model. This approach continues in multiple iterations until the convergence criterion is met. When the performance criterion is achieved, the iterative loop terminates and the final machine performance is obtained. This approach includes only one fluid (e.g. rotating air) and models the impact from the other coolant (e.g. cooling water) from the HTC-LUT with a pre-determined range of coolant flow rates. Thus, the proposed approach converges rapidly as compared to the case where both fluids are modeled in CFD.

### B. TEMPERATURE-DEPENDENT MATERIAL PROPERTIES

Since the physical properties of materials depend mainly on the operating temperature, the EM-CFD coupling is established based on temperature-dependent materials of the magnet (NdFeB), stator windings (copper), stator/rotor (steel) and frame (cast-iron). These temperature-dependent characteristics are incorporated in the EM model. The material properties used in the analysis are outlined in Table 4, where $\rho$ is the mass density, $c_p$ is the specific heat, and $\lambda$ is the thermal conductivity. The initial temperature for all machine parts is kept at 100°C.

A scalable temperature-dependent *B-H* characteristics for the magnet material is applied as shown in Fig. 20 and it is

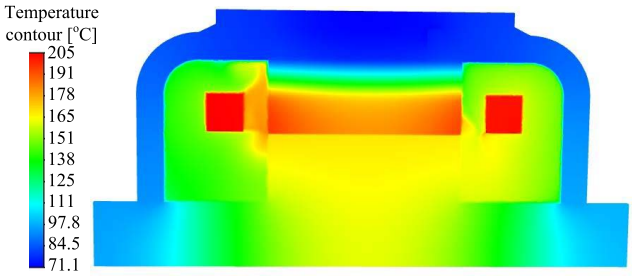


**FIGURE 21. Temperature gradient contour of EM-CFD coupling approach at the current density of 1.5 p.u. and flow rate of 12 LPM.**

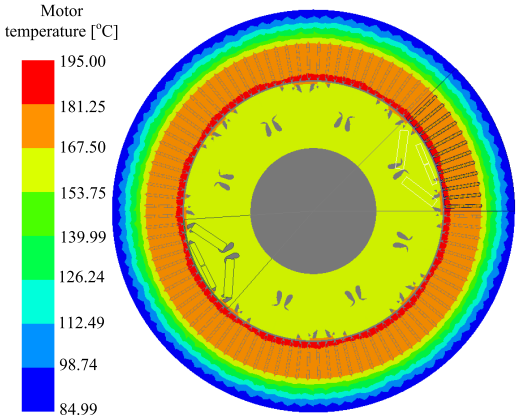


**FIGURE 22. Temperature distribution of EM-CFD coupling approach at the current density of 1.5 p.u.**

automatically updated based on the input feedback temperature obtained from the CFD analysis. As the magnet temperature increases, both the magnet remanent flux density and coercivity decrease which results in shrinking *B-H* curves. This makes the magnets more prone to demagnetization. As the magnet flux density reduces with temperature, the air-gap flux density decreases accordingly. Since the motor losses depend on the air-gap flux density, the corresponding updated magnet *B-H* curve is then utilized to calculate the new iron losses for the EM-CFD two-way coupled model. Additionally, the conductivity of the copper and lamination steel decrease with temperature.

### C. RESULTS AND DISCUSSION

The proposed EM-CFD coupling method is carried out for several current density values. The current density targeted for continuous operation is defined as 1 p.u. The initial temperature for all machine components is 100°C. The ambient temperature was defined as 25°C. The coolant flow rate was set at 12 LPM and initial inlet temperature of the coolant is defined as 70°.

Fig. 21 shows the temperature gradient in CFD post-processing and Fig. 22 show the temperature contour plot in the EM model after being updated with the thermal feedback. Figs. 23–25 show the average torque, iron loss, and copper loss at different current densities.

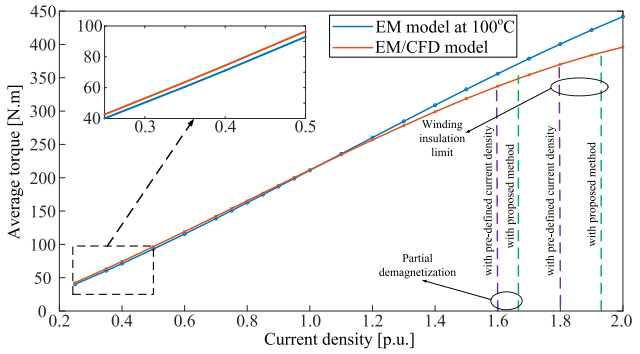


**FIGURE 23.** Average torque versus current density for EM and EM-CFD coupling models at the base speed and 12 liters/min inlet flow rate.

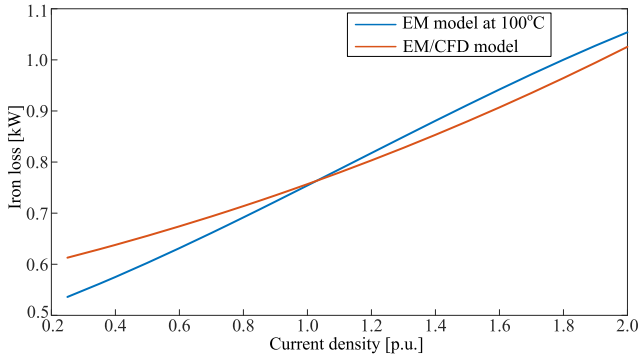


**FIGURE 24.** Core loss versus current density for EM and EM-CFD coupling models at the base speed and 12 liters/min inlet flow rate.

The proposed approach calculates the non-homogeneous temperature across the rotor and stator surface and it is used to determine the current density that corresponds to the maximum operating temperature.

As compared to the conventional method with a pre-defined current density, new partial demagnetization and winding insulation limits are set with the proposed coupling method, as shown in Fig. 23. The new limits are higher than the ones with the conventional method where a pre-defined current density is used. From Fig. 23, it can be observed that the average torque increases linearly with the increase in the current density if a constant temperature is considered. However, with a non-homogenous temperature distribution calculated from the proposed coupling approach, the average torque starts to decrease when the temperature exceeds 100°C. This is due to the partial demagnetization of the magnets.

Fig. 24 shows the total iron loss as a function of current density. At higher current density values, iron losses calculated from the EM/CFD model is lower than the ones calculated from the EM model with uniform temperature. This difference is related to the occurrence of partial demagnetization. As the temperature increases, the magnetic flux density and, hence, the average torque drops due to partial demagnetization. Lower magnetic flux density level results in lower iron loss as depicted in Fig. 24.

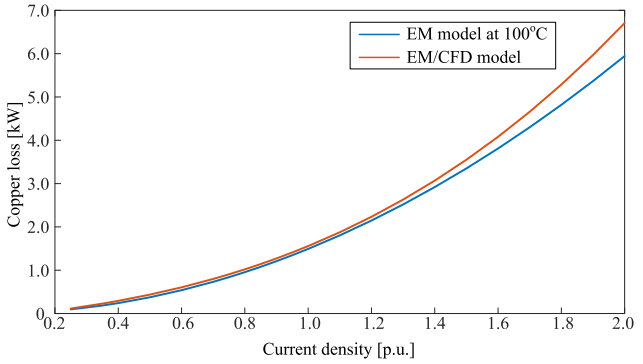


**FIGURE 25.** Copper loss versus current density for EM and EM-CFD coupling models at the base speed and 12 liters/min inlet flow rate.

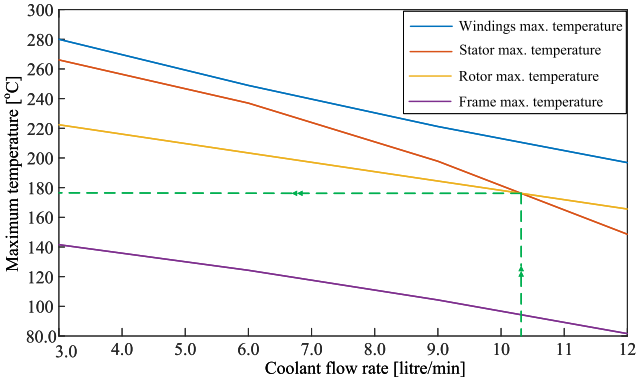


**FIGURE 26.** Maximum temperature with respect to inlet flow rate at the current density of 1.5 p.u.

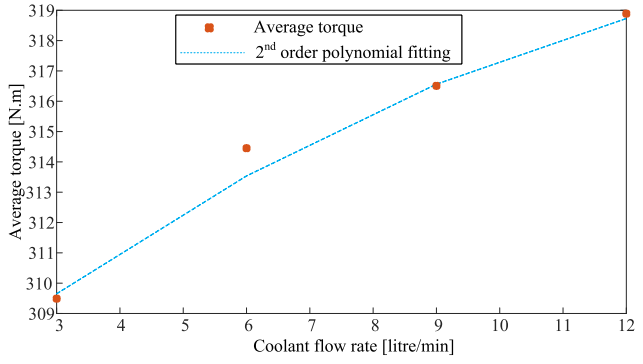


**FIGURE 27.** Average torque versus inlet flow rate at the current density of 1.5 p.u.

On the contrary, as demonstrated in Fig. 25, copper loss increases as the current density increases. Fig. 25 shows the copper loss at the base speed. Hence, dc copper loss is the dominant loss component. At lower current densities, the difference in copper loss is small since the current is small. However, at higher current densities, the difference becomes significant since the resistivity of the copper increases with temperature.

Fig. 26 shows the maximum temperature of different motor parts at different coolant flow rates. With the increase in

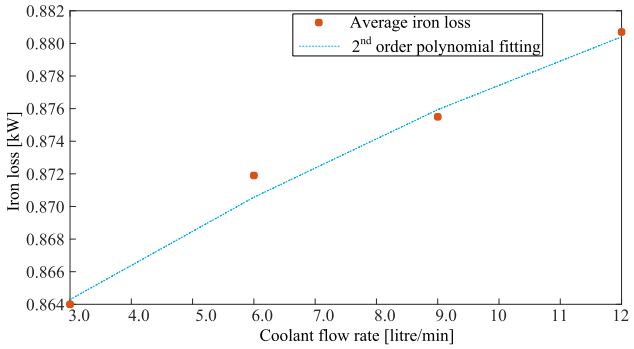


**FIGURE 28.** Average iron loss versus inlet flow rate at the base speed at the current density of 1.5 p.u.

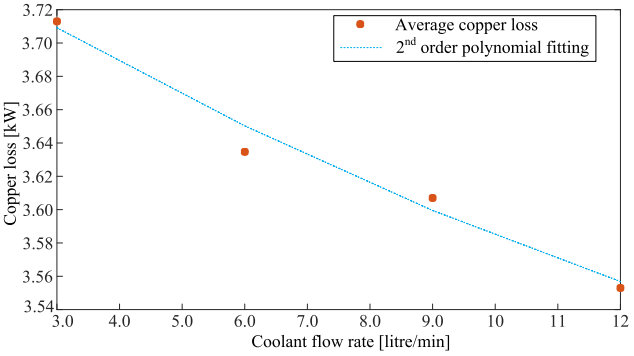


**FIGURE 29.** Average copper loss versus inlet flow rate at the base speed at the current density of 1.5 p.u.

**TABLE 5.** Comparison of temperature rise between EM-CFD coupling and LPTN analytical approaches.

| Motor component | EM-CFD Approach | LPTN Approach | Discrepancy (%) |
|---|---|---|---|
| Windings | 135.29 | 130.40 | 3.61 |
| Stator | 126.70 | 118.70 | 7.10 |
| Rotor | 100.47 | 91.30 | 9.12 |
| Magnets | 98.2 | 95.60 | 2.64 |
| Frame | 27.02 | 19.40 | 29.53 |
| Shaft | 94.07 | 79.30 | 15.70 |

the inlet flow rate, the maximum temperature of the motor components decrease steadily. However, beyond 10.3 LPM flow rate, which is the intersection point between the stator and rotor maximum temperature curves as depicted in Fig. 26, the stator surface temperature starts to fall below the rotor surface temperature. This indicates that at 10.3 LPM, the convective HTC between the stator and the cooling jacket is higher. That enables a higher dissipation rate of the power loss and, hence, it results in a lower stator surface temperature than the rotor. This is why the demagnetization limit, calculated with the proposed method in Fig. 23, does not change as much as the winding insulation limit. Figs. 27–29 show the average torque, iron loss, and copper loss at different inlet flow rates at 1.5 p.u. current density. As the flow rate increases, the temperature decreases and, hence, the average torque increase. Copper loss reduces with the increase in flow rate,

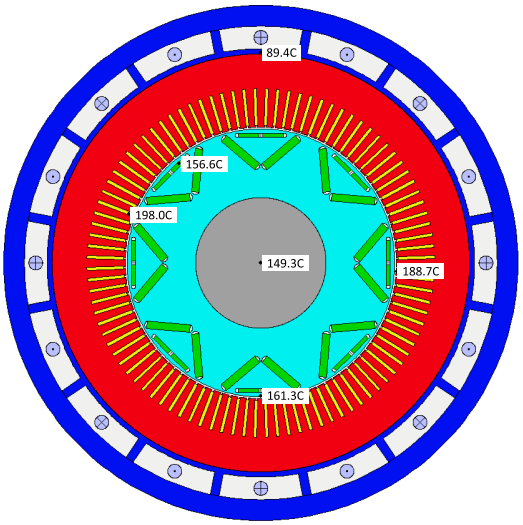


**FIGURE 30.** Cross-sectional view of the LPTN model of the motor with the maximum temperature of different components.

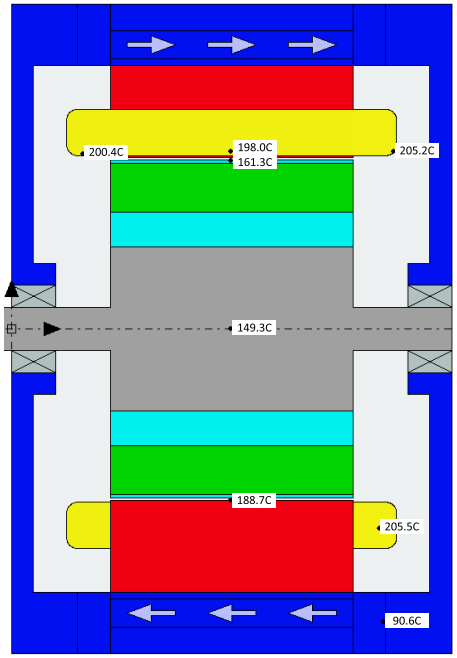


**FIGURE 31.** Axial view for the LPTN model of the motor with maximum temperature of different components.

because lower temperature results in lower phase resistance. The iron loss increases, as the flux density increases with lower temperature.

## VI. VERIFICATION WITH LUMPED PARAMETER THERMAL NETWORK

The lumped parameter thermal network (LPTN) is an analytical way to determine the thermal response of electric motors. An LPTN is analogous to an electric circuit where the voltage is represented by the temperature difference, the current by the heat transfer rate, and the electrical resistance by the thermal resistance. However, the thermal time

constant is denoted by a thermal capacitance to determine how quickly the temperature rises based on the component's thermal energy storage. MotorCAD software is used for the LPTN model of the motor. The heat transfer coefficients calculated from the proposed EM-CFD coupling approach are applied to the water jacket in the LPTN model to calculate its thermal resistance. The results from the proposed EM-CFD coupling approach and the LPTN analytical approach are compared at a current density of 1.5 p.u. and an inlet flow rate of 12 LPM. Fig. 30 shows cross-sectional view of the motor with the maximum temperature of each component. Fig. 31 shows the axial view for the LPTN model of the motor to point out the maximum temperature of the end-windings. Table 5 compares the temperature rise results calculated from the proposed EM-CFD coupling approach and the LPTN approach. The results from the two approaches are in close agreement. The highest deviation is 29.53% and it is for the frame.

It is worth mentioning that the bearings and their corresponding bearing plates are automatically taken into account when building the MotorCAD model as indicated in Fig. 31. However, for the model simplicity, those components have not been considered in the CFD modeling. Therefore, the rotor temperature calculated in MotorCAD in Fig. 31 is lower than the CFD results in Fig. 22. The bearing and the bearing plates provide a direct thermal path between the rotor and the motor housing and, hence, help reduce the rotor temperature.

The results from the LPTN analytical approach verify that the proposed method show close agreement with the EM-CFD coupling approach. From the thermal management standpoint, for the analyzed motor, improvements on the cooling system could be applied and the cooling channels or additional cooling on the end turns could be applied to reduce the temperature rise and avoid possible degradation of coil and slot insulation.

## VII. CONCLUSION

This paper presents a coupled electromagnetic-computational fluid dynamics (EM-CFD) analysis methodology for an electric motor application where a heat transfer coefficient look-up table (HTC-LUT) is adopted for the water-cooling jacket. This methodology enables decoupling of the fluid-to-fluid interaction between the internal rotating air and the cooling water and, hence, reduces the computational time. The proposed EM-CFD coupling methodology facilitates a way to design and improve the cooling methodology so that the electromagnetic performance targets can be met and a high power density can be achieved. Electromagnetic losses and temperature-dependent material properties provide a link between the EM and CFD thermal analyses. The generated HTC-LUT is utilized as a surrogate for the main CFD simulation to determine the temperature rise of different motor components and their HTCs. A correlation between coolant flow rate, motor speed, local air velocity and heat transfer coefficients has been established. It has been demonstrated that the stator surface temperature starts to drop below the rotor surface temperature when inlet flow rate exceeds 10.3 LPM. This means that the HTC of the stator surface is capable of dissipating more losses as compared to the rotor. The LPTN analytical approach is used to verify the proposed approach and the results show close agreement with the EM-CFD coupling approach.

## ACKNOWLEDGMENT

The authors would like to thank the ANSYS for their support with ANSYS Maxwell, CFD (Fluent), and ANSYS MotorCAD software in this research.

## REFERENCES

[1] (2013). U. S. Department of Energy. *electrical and Electronics Technical Team Roadmap*. (Oct. 2017). [Online]. Available: https://www.energy.gov/
[2] R. Yang, N. Schofield, N. Zhao, and A. Emadi, "Dual three-phase permanent magnet synchronous machine investigation for battery electric vehicle power-trains," *J. Eng.*, vol. 2019, no. 17, pp. 3981–3985, Jun. 2019.
[3] G. Feng, C. Lai, M. Kelly, and N. C. Kar, "Dual three-phase PMSM torque modeling and maximum torque per peak current control through optimized harmonic current injection," *IEEE Trans. Ind. Electron.*, vol. 66, no. 5, pp. 3356–3368, May 2019.
[4] W. Tong, *Mechanical Design of Electric Motors*. Boca Raton, FL, USA: CRC Press, 2014.
[5] R. Wrobel, J. Goss, A. Mlot, and P. H. Mellor, "Design considerations of a brushless open-slot radial-flux PM hub motor," *IEEE Trans. Ind. Appl.*, vol. 50, no. 3, pp. 1757–1767, May 2014.
[6] S. A. Semidey, Y. Duan, J. R. Mayor, R. G. Harley, and T. G. Habetler, "Optimal electromagnetic-thermo-mechanical integrated design candidate search and selection for surface-mount permanent-magnet machines considering load profiles," *IEEE Trans. Ind. Appl.*, vol. 47, no. 6, pp. 2460–2468, Nov. 2011.
[7] J. Wang and D. Howe, "Design optimization of radially magnetized, iron-cored, tubular permanent-magnet machines and drive systems," *IEEE Trans. Magn.*, vol. 40, no. 5, pp. 3262–3277, Sep. 2004.
[8] L. Jolly, M. A. Jabbar, and L. Qinghua, "Optimization of the constant power speed range of a saturated permanent-magnet synchronous motor," *IEEE Trans. Ind. Appl.*, vol. 42, no. 4, pp. 1024–1030, Jul./Aug. 2006.
[9] L. Encica, J. J. H. Paulides, E. A. Lomonova, and A. J. A. Vandenput, "Electromagnetic and thermal design of a linear actuator using output polynomial space mapping," *IEEE Trans. Ind. Appl.*, vol. 44, no. 2, pp. 534–542, Mar. 2008.
[10] S. Wiak, A. Krawczyk, and I. Dolezel, "Optimum design of linear motor for weight reduction using response surface methodology," *Adv. Comput. Techn. Appl. Electromagn.*, vol. 30, p. 184, Jul. 2008.
[11] A. Sarikhani and O. Mohammed, "A multi-physics multi-objective optimal design approach of PM synchronous machines," in *Proc. Int. Conf. Electr. Mach. (ICEM)*, Berlin, Germany, Sep. 2014, pp. 968–974.
[12] M. Markovic and Y. Perriard, "Optimization design of a segmented Halbach permanent-magnet motor using an analytical model," *IEEE Trans. Magn.*, vol. 45, no. 7, pp. 2955–2960, Jul. 2009.
[13] N. Bracikowski, M. Hecquet, P. Brochet, and S. V. Shirinskii, "Multiphysics modeling of a permanent magnet synchronous machine by using lumped models," *IEEE Trans. Ind. Electron.*, vol. 59, no. 6, pp. 2426–2437, Sep. 2011.
[14] A. Rodriguez, D. Gómez, I. Villar, A. López-de Heredia, and I. Etxeberria-Otadui, "Improved analytical multiphysical modeling of a surface pmsm," in *Proc. Int. Conf. Electr. Mach. (ICEM)*, Berlin, Germany, Sep. 2014, pp. 1224–1230.
[15] J. Legranger, G. Friedrich, S. Vivier, and J. C. Mipo, "Combination of finite-element and analytical models in the optimal multidomain design of machines: Application to an interior permanent-magnet starter generator," *IEEE Trans. Ind. Appl.*, vol. 46, no. 1, pp. 232–239, Jan. 2009.
[16] X. Jannot, J.-C. Vannier, C. Marchand, M. Gabsi, J. Saint-Michel, and D. Sadarnac, "Multiphysic modeling of a high-speed interior permanent-magnet synchronous machine for a multiobjective optimal design," *IEEE Trans. Energy Convers.*, vol. 26, no. 2, pp. 457–467, Jun. 2010.
[17] P. Akiki, M. H. Hassan, M. Bensetti, P. Dessante, J.-C. Vannier, D. Prieto, and M. McClelland, "Multiphysics design of a V-shape IPM motor," *IEEE Trans. Energy Convers.*, vol. 33, no. 3, pp. 1141–1153, Sep. 2018.

[18] W. Jiang and T. M. Jahns, "Coupled electromagnetic–thermal analysis of electric machines including transient operation based on finite-element techniques," *IEEE Trans. Ind. Appl.*, vol. 51, no. 2, pp. 1880–1889, Mar./Apr. 2014.
[19] B. Bilgin, J. Liang, M. V. Terzic, J. Dong, R. Rodriguez, E. Trickett, and A. Emadi, "Modeling and analysis of electric motors: State-of-the-art review," *IEEE Trans. Transport. Electrific.*, vol. 5, no. 3, pp. 602–617, Sep. 2019.
[20] Y. Wang, J. Taylor, and B. Bilgin, "Comparative study of three-phase and dual three-phase machines considering PWM effect," in *Proc. IEEE Energy Convers. Congr. Expo. (ECCE)*, Vancouver, BC, Canada, Oct. 2021, pp. 4157–4163.
[21] M. Ibrahim and P. Pillay, "Core loss prediction in electrical machine laminations considering skin effect and minor hysteresis loops," *IEEE Trans. Ind. Appl.*, vol. 49, no. 5, pp. 2061–2068, Sep. 2013.
[22] X. Yang, A. Fatemi, T. Nehl, L. Hao, W. Zeng, and S. Parrish, "Comparative study of three stator cooling jackets for electric machine of mild hybrid vehicle," *IEEE Trans. Ind. Appl.*, vol. 57, no. 2, pp. 1193–1201, Mar. 2021.
[23] S. Jones-Jackson, R. Rodriguez, E. Sayed, C. Goldstein, C. Mak, A. Callegaro, M. Goykhman, and A. Emadi, "Design and analysis of stator cooling channels for an axial-flux permanent magnet machine," in *Proc. IEEE Transp. Electrific. Conf. Expo (ITEC)*, Chicago, IL, USA, Jun. 2021, pp. 272–277.
[24] I. Zaher, R. Rodriguez, E. Sayed, A. Callegaro, M. Goykhman, and A. Emadi, "Effect of rotor geometry on rotor air cooling of a ventilated axial-flux permanent magnet machine," in *Proc. IEEE Transp. Electrific. Conf. Expo (ITEC)*, Chicago, IL, USA, Jun. 2021, pp. 77–82.
[25] E. Sozer, C. Brehm, and C. C. Kiris, "Gradient calculation methods on arbitrary polyhedral unstructured meshes for cell-centered CFD solvers," in *Proc. 52nd Aerosp. Sci. Meeting*, National Harbor, MD, USA, Jan. 2014, pp. 1434–1440.
[26] *Ansys Fluent Theory Guide*, A. F. Documentation, ANSYS Help, Canonsburg, PA, USA, 2016.
[27] L. D. Di Angelo, F. Duronio, A. D. De Vita, and A. D. Di Mascio, "Cartesian mesh generation with local refinement for immersed boundary approaches," *J. Mar. Sci. Eng.*, vol. 9, no. 6, p. 572, May 2021.
[28] P. Kiš and H. Herwig, "The near wall physics and wall functions for turbulent natural convection," *Int. J. Heat Mass Transf.*, vol. 55, nos. 9–10, pp. 2625–2635, Apr. 2012.
[29] H. Schlichting and K. Gersten, *Boundary-Layer Theory*. Berlin, Germany: Springer, 2003.
[30] J. Matsson, *An Introduction to ANSYS Fluent 2020*. Mission, KS, USA: SDC Publications, 2020.
[31] T. L. Bergman, F. P. Incropera, D. P. DeWitt, and A. S. Lavine, *Fundamentals of Heat and Mass Transfer*. Hoboken, NJ, USA: Wiley, 2011.
[32] H. K. Versteeg and W. Malalasekera, *An Introduction to Computational Fluid Dynamics: The Finite Volume Method*. London, U.K.: Pearson, 2007.
[33] P. Gullberg and R. Sengupta, "Axial fan performance predictions in CFD, comparison of MRF and sliding mesh with experiments," SAE Tech. Paper, Detroit, MI, USA, Tech. Rep. 0652, 2011.
[34] A. Tovar-Barranco, A. Lopez-de-Heredia, I. Villar, and F. Briz, "Modeling of end-space convection heat-transfer for internal and external rotor PMSMs with fractional-slot concentrated windings," *IEEE Trans. Ind. Electron.*, vol. 68, no. 3, pp. 1928–1937, Mar. 2021.

**AHMED S. ABDELRAHMAN** (Member, IEEE) received the B.Sc. and M.Sc. degrees in electrical engineering from Cairo University, Cairo, Egypt, in 2010 and 2013, respectively, and the Ph.D. degree in electrical engineering from Ontario Tech University, in 2019.

Previously, he worked as a Postdoctoral Research Fellow at the McMaster Automotive Resource Centre (MARC), Electric Machine Design Research Thrust Area (EM-RTA) Team, McMaster University, in collaboration with Stellantis N. V., for the development of next-generation hybrid-electric drivetrains for vehicles. He is currently a Principal Engineer with Enedym Inc., Hamilton, ON, Canada. He has authored or coauthored more than five journals and 14 conference papers. His current research interests include electric machines design, thermal analysis via computational fluid dynamics (CFD), acoustic noise and vibration analysis and mitigation, structural/stress analysis, and multi-physics analysis and simulation for SRM and IPM machines.

**BERKER BILGIN** (Senior Member, IEEE) received the Ph.D. degree in electrical engineering from the Illinois Institute of Technology, Chicago, IL, USA, in 2011, and the M.B.A. degree from the DeGroote School of Business, McMaster University, Hamilton, ON, Canada, in 2018.

He is currently an Assistant Professor with the Department of Electrical and Computer Engineering (ECE), McMaster University. He is also the Co-Founder and the Vice President of Engineering of Enedym Inc., Hamilton, ON, Canada, which is a spin-off company of McMaster University. He specializes in electric machines, electric motor drives (EMDs), advanced controls and software, and virtual engineering. He has authored or coauthored 131 journals and conference papers and three book chapters. He is the principal inventor/a co-inventor of ten patents and pending patent applications. He is the Lead Editor and the author of the textbook titled *SRM Drives: Fundamentals to Applications*. His current research interests include electric machines, switched reluctance motor (SRM) drives, acoustic noise and vibration analysis and reduction, and power electronics, and EMDs.

Dr. Bilgin was the Elected General Chair of the 2016 IEEE Transportation Electrification Conference and Expo (ITEC). He also serves as an Associate Editor for the IEEE TRANSACTIONS ON TRANSPORTATION ELECTRIFICATION.